sustainability

MDPI

Article

Direct Measurement of Static and Dynamic Contact Angles Using a Random Micromodel Considering Geological CO_2 Sequestration

Mohammad Jafari [1] and Jongwon Jung [2,*]

[1] Department of Civil and Environmental Engineering, Louisiana State University, Baton Rouge, LA 70808, USA; mjafar3@lsu.edu

[2] School of Civil Engineering, Chungbuk National University, Chungdae-ro 1, Seowon-Gu, Cheongju, Chungbuk 28644, Korea

* Correspondence: jjung@chungbuk.ac.kr; Tel.: +82-43-261-2405

Received: 10 October 2017; Accepted: 9 December 2017; Published: 16 December 2017

Abstract: The pore-level two-phase fluids flow mechanism needs to be understood for geological CO_2 sequestration as a solution to mitigate anthropogenic emission of carbon dioxide. Capillary pressure at the interface of water–CO_2 influences CO_2 injectability, capacity, and safety of the storage system. Wettability usually measured by contact angle is always a major uncertainty source among important parameters affecting capillary pressure. The contact angle is mostly determined on a flat surface as a representative of the rock surface. However, a simple and precise method for determining in situ contact angle at pore-scale is needed to simulate fluids flow in porous media. Recent progresses in X-ray tomography technique has provided a robust way to measure in situ contact angle of rocks. However, slow imaging and complicated image processing make it impossible to measure dynamic contact angle. In the present paper, a series of static and dynamic contact angles as well as contact angles on flat surface were measured inside a micromodel with random pattern of channels under high pressure condition. Our results showed a wide range of pore-scale contact angles, implying complexity of the pore-scale contact angle even in a highly smooth and chemically homogenous glass micromodel. Receding contact angle (RCA) showed more reproducibility compared to advancing contact angle (ACA) and static contact angle (SCA) for repeating tests and during both drainage and imbibition. With decreasing pore size, RCA was increased. The hysteresis of the dynamic contact angle (ACA–RCA) was higher at pressure of one megapascal in comparison with that at eight megapascals. The CO_2 bubble had higher mobility at higher depths due to lower hysteresis which is unfavorable. CO_2 bubbles resting on the flat surface of the micromodel channel showed a wide range of contact angles. They were much higher than reported contact angle values observed with sessile drop or captive bubble tests on a flat plate of glass in previous reports. This implies that more precaution is required when estimating capillary pressure and leakage risk.

Keywords: advance contact angle; receding contact angle; static contact angle; dynamic contact angle; CO_2 sequestration

1. Introduction

Despite all the efforts towards developing renewable energy, fossil fuels are still the main source of energy. CO_2 emission is an inevitable consequence of fossil fuel combustion. Geological CO_2 sequestration has been recently developed as a promising method to decrease anthropogenic CO_2 emission. The main idea of this method is to separate CO_2 (i.e., CO_2 from other gases in main emitters such as fossil fuel-based power plants and other industrial units), transfer it by pipelines or tanks, and finally inject it into underground layers such as depleted oil and gas reservoirs, deep saline aquifers,

deep unmineable coal beds, and methane hydrate bearing sediments. This injected CO_2 is trapped underground by two short-term mechanisms: structural trapping and capillary (or residual) trapping. In the long-term, two safer mechanisms, solubility trapping and mineral trapping, are activated to trap CO_2 underground [1–5]. The two short-term mechanisms are highly important. They are the focus of this work because they guarantee prompt safety of storage. In addition, they can trigger the safer long-term mechanisms.

Capillary force is the main factor governing the multiphase flow in porous media along with viscos and inertial forces. Connected CO_2 plume is trapped under a sealing caprock by capillary pressure during structural trapping. Disconnected CO_2 bubbles are immobilized among rock pores by water/brine for residual trapping as a result of hysteresis and local capillary trapping [6]. Capillary or residual trapping is the more favorable between the abovementioned two short-term storage trappings. In structural trapping, a pileup and thick layer of connected CO_2 causes an enormous uplift pressure under a sealing caprock. Any phenomenon affecting the integrity of the sealing caprock layer can dramatically increase the risk of an abrupt leakage. However, in capillary (or residual) trapping, disconnected bubbles of CO_2 are immobilized in a distributed form in rock pores by local capillary pressure difference. Thus, capillary (or residual) trapping is much safer than structural trapping. Also, capillary trapping provides more chance for disconnected CO_2 bubbles to be dissolved into water/brine, consequently increasing the rate of mineral trapping [7]. The Inter-governmental Panel on Climate Change (IPCC) has also emphasized the importance of capillary (or residual) trapping for safe and economical geological CO_2 storage [8].

Wettability is the most crucial factor among various parameters affecting capillary pressure because of its complexity and uncertainty. Wettability is often quantified by measurement of contact angle which is the angle between the water–CO_2 interface and rock surface measured through the denser phase (water here). The contact angle can be categorized into different types. If the water–CO_2 interface has no motion, the contact angle is called a static contact angle. A dynamic contact angle is measured when the interface has a motion on the solid (i.e., rock or soil) surface and is categorized as receding and advancing based on the direction of the fluids interface.

Any value of the abovementioned contact angle should be considered in a CO_2 storage process. For example, when CO_2 pushes water during initial injection, a receding contact angle should be considered. When some portion of CO_2 with density lower than water migrates upward and reaches under caprock and tends to penetrate into the sealing caprock, a receding contact angle should be considered. After completing CO_2 injection, water imbibes into the CO_2 storage by pressure rearrangement which traps some portion of CO_2 as the form of disconnected bubbles. Each side of the CO_2 bubble is under advancing or receding condition depending on the direction of bubble motion. Contact angle is under static condition when the motion of the CO_2 bubble stops.

The pore-scale numerical model of fluids flow provides considerable information, such as fluid configuration during and after injection, capillary breakthrough pressure, and relative permeability. These can be applied to estimate the capacity and safety of a storage. A robust pore-scale numerical model requires knowledge of in situ contact angle in different modes. However, previous models suffer uncertainty originating from the lack of a direct contact angle measurement inside pores [9]. Technical drawbacks have inhibited researchers from measuring the contact angle inside a rock pore directly. For many years, contact angles have been measured indirectly using methods such as capillary rise or pressure measurements using a capillary tube or thin plate filled with powder or bids of a certain material based on Lucas–Washburn and Young–Laplace equations, capillary pressure curves, USBM (United States Bureau of Mines), or Amott methods [10–17]. These indirect methods only yielded a statistical sense of microscopic behavior of rock or soil samples. Values of in-situ contact angles and local capillary pressure are not distinguishable [9]. In a different approach, static and dynamic contact angles have been vastly measured on a flat surface representing a specific mineral surface (i.e., silica, mica, or natural rock) using various methods such as sessile drop, captive bubble, Wilhelmy plate, and dual-drop dual-crystal (DDDC) methods [18–29].

High discrepancies in contact angles measured in literature have been observed. This is caused by the use of different measurement methods, rock or mineral surface imperfections, and surface cleaning methods [19]. Whether the contact angle on a flat surface can properly represent wettability inside of a porous medium pore has been a great concern. Microscopic roughness and chemical heterogeneity of pore walls originate from different in-situ minerals and curvature of pore walls, making the contact angle measured on a smooth flat surface an unreliable one for pores inside porous media [30].

Lin et al. [31] had shown a good agreement between receding contact angles both on a flat surface and inside a capillary tube for very smooth polymers. However, Li et al. [32] have recently reported that water contact angle on a flat glass sheet can be different from a contact angle inside of a capillary tube with the same material (the inner diameter of the tube ranged from 100 to 1000 μm). The importance of more realistic wettability in predicting multi-phase flow behavior requires the development of new techniques for measuring contact angle at pore-scale level. The recent X-ray computed tomography (micro-CT) method has provided a powerful tool to study pore and micro-scale characterization of rocks and multiphase fluid flow mechanisms, including pore structure morphology and local capillary pressure measurement [33–37]. Using the micro-CT technique, it is really difficult to measure dynamic contact angles due to the slow imaging process [30]. Thus, static contact angles have been measured with rocks, sand packs, and glass bids, showing a wide range of contact angles at pore level. The wide range of static contact angles are due to the following: (1) pore topology, hysteresis, surface chemical and physical heterogeneity, and injection patterns (i.e., drainage and imbibition) [9,30,33,38–40]; (2) relaxation of contact angle [30]; and (3) low resolution of images. Thus, Scanziani et al. [9] have proposed an "effective contact angle" measurement using fluid–fluid interface curvature instead of "true contact angle" at the contact line of fluids and rock surface. When CO_2 injection is stopped, the movement of the CO_2 interface front stops and a static contact angle can be measured. At this moment, the interface is approaching an equilibrium condition called the relaxation of contact angle [30].

In present study, considering in-situ CO_2 flow in porous media, contact angles are directly measured inside pores using a high-pressure micromodel with random pore network pattern. The transparent micromodel provides high resolution observation of fluids interface, and imaging is fast enough to capture dynamic contact angle. To the best of the authors' knowledge, it is the first pore-scale dynamic contact angle measurement when the interface of the fluids is moving inside the channels of a randomly pattern micromodel. Moreover, the preferential behavior of wetting and non-wetting fluids in occupying different pores and throat size is also observed by the used micromodel which is not achievable with capillary tube measurement. This study is an effort to determine the effect of pore size on wettability in a micromodel with relatively homogenous material and simple geometry in comparison with a real rock core. The results of this study can provide valuable information regarding pore-scale wettability behavior of porous media that can be applied in simulation of two-phase immiscible fluid flow for geological CO_2 sequestration or other projects involved with injection of CO_2 underground.

2. Materials and Methods

2.1. Micromodel

High-pressure microchips (Micronit Microfluidics, Enschede, The Netherlands) with a random network as a micromodel is used. These microchips are made of a borosilicate glass with a network dimension of 20 × 10 mm encompassed in a polymer (PP) cartridge with dimension of 75 × 25 mm. The micromodel consists of two layers of glass with thickness of 1100 and 700 μm. One of these layers is etched with a random pattern of square channels. These channels exist at different widths (47, 67, 87, 107, and 127 μm) with the same depth of 20 μm.

2.2. Experimental Set-Up

The micromodel is horizontally placed on adjustable jack stages. A precise syringe pump (Kats Scientific, NE-1010, Kats Enterprises, Denton, TX, USA) controlling a high-pressure steel syringe (KD Scientific, 2.5 mL) is used to drain and inject water into the micromodel. The stainless-steel syringe is connected to one side of micromodel with a transparent tubing. The high-pressure transparent tubing is used to observe the interface between CO_2 and water. On the other side, the micromodel is connected to a precise-high-pressure ISCO pump (500 HP, Teledyne ISCO, NE, USA) by another transparent tubing. A digital camera records a video during fluid injection into the micromodel. Pressure and temperature data are collected by an OMEGA PX309-3kGV pressure transducer (having 20 MPa capacity and accuracy of 0.25%) and a T-type (Copper/Constantan, OMEGA, Norwalk, CT, USA) thermocouple (OMEGA, Norwalk, CT, USA), respectively. The sensor information is recorded using a data logger.

2.3. Experimental Procedure

Before starting tests, the micromodel is cleaned by injecting 5 mL absolute ethanol (Mallinckodt Baker, ACS reagent grade,) and then 30 mL deionized water. The micromodel is dried in an oven at 120 °C for 48 h. The cleaned micromodel is assembled in the system (Figure 1). CO_2 is used to flush the whole system to remove air in the micromodel, tubing, and syringe. The syringe is filled with deionized water and connected to the micromodel. Using the syringe pump, the micromodel is saturated with deionized water (DI). The ISCO pump is then used to pressurize the system to target pressures (1 or 8 MPa) gradually. The water–CO_2 interface is placed in the tubing at the ISCO pump side. The system is left under constant pressure for 24 h to reach thermodynamic equilibrium.

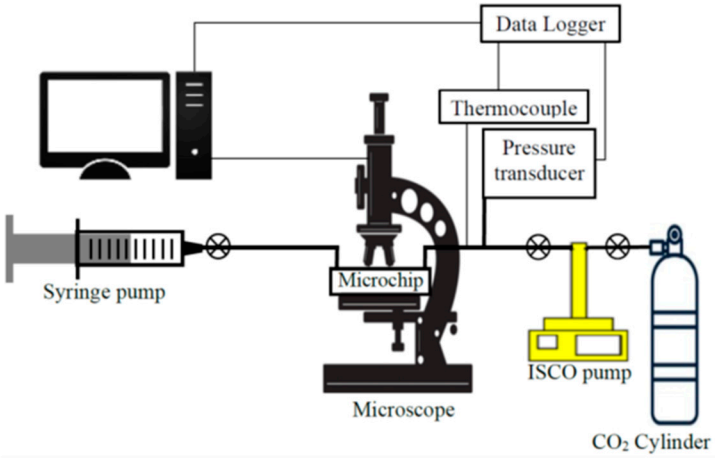

Figure 1. Schematic design for contact angle measurement using a micromodel.

Water is withdrawn with a syringe pump at a constant flow rate of 0.1 µL/min while the pressure remains constant by the ISCO pump. Water flow-out continued until CO_2 percolates into the micromodel. After CO_2 percolation, water withdrawal continues for ~100 pore volumes. The amount of CO_2 in the micromodel represents the drainage CO_2 saturation. Water is then injected into the micromodel with a constant flow rate of 0.1 µL/min which simulates the imbibition process. Water passes through the micromodel and then reaches the tubing at the ISCO pump side. The amount of remaining CO_2 in the micromodel represented trapped CO_2 saturation. An inverted microscope is used to obtain both photo and video from these micromodel channels during the test. Table 1 shows the different test conditions conducted in this study.

Table 1. Test condition.

Test	Pressure (MPa)	Temperature (°C)	Water Withdrawal Flow Rate (μL/min) During Drainage	Water Injection Flow Rate (μL/min) During Imbibition	CA Measurement Type
Type 1	1	21	0.1	0.1	Static & dynamic
Type 2	8	21	0.1	0.1	Static & dynamic

2.4. Contact Angle Measurement

Static contact angles (SCAs) are measured from photos or videos when the interface has no motion. Dynamic contact angles are measured using paused video when the interface is moving. Receding contact angles (RCA) and advancing contact angles (ACA) are observed when CO_2 displaces water and when water displaces CO_2, respectively. The contact angle measured from the prepared pictures using AutoCAD software. The contact angle measurement accuracy by AutoCAD was verified by comparing values with results from an image processing software (ImageJ with a plugin function (Contact Angle)). The accuracy and repeatability of contact angle measurement with ImageJ have been verified in [41,42].

3. Results and Discussion

Figure 2 shows how the RCA and ACA in the micromodel are measured in same channel. When CO_2 displaces water in the micromodel, receding contact angles are observed (Figure 2a). When water displaces CO_2, advancing contact angles are measured (Figure 2b). Images are captured while the interface had motion. Pore throat size is 127 μm in Figure 2a. Results show that the advancing contact angle is considerably higher than the receding contact angle in the same pore throat, consistent with previous studies [18,22,43–45]. The difference between ACA and RCA is attributed to the blemishes on non-ideal surfaces which results in pinning the interfaces to the solid surface [46]. Various RCAs and ACAs at throat size of 47 μm in the micromodel are also shown in Figure 2c,d, respectively.

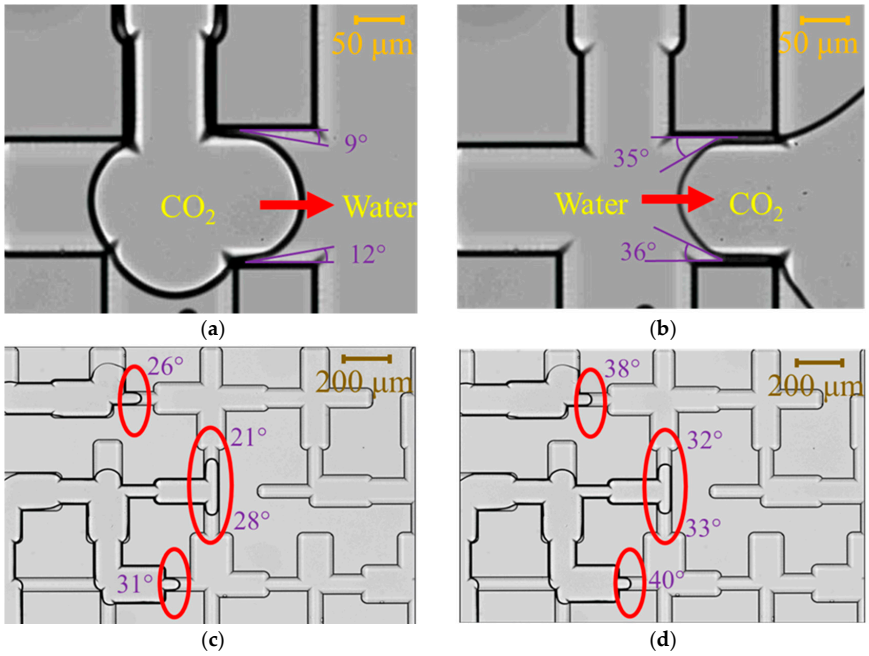

Figure 2. Contact angle measurement in the micromodel at pressure of eight megapascals. (**a**) Receding contact angle at pore throat size of 127 μm; (**b**) Advancing contact angle at pore throat size of 127 μm; (**c**) Receding contact angles at pore throat size of 47 μm; (**d**) Advancing contact angles at pore throat size of 47 μm.

3.1. Dynamic Contact Angle

Pinning effect of a triple line. Figure 3 shows receding and advancing contact angles changing with various pore throat sizes (ranged from 47 μm to 127 μm) at pressure of eight megapascals for two different tests. Results show that for the repeated tests, receding contact angles are more reproducible compared with advancing contact angles (Figure 3). For example, when the pore throat size is 87 μm, standard deviations of RCA and ACA are ±4° and ±16°, respectively. This could be due to the pinning effect of a triple line during the imbibition process. Triple line, which is also called three-phase line, is the line that the three phases of the liquid, gaseous, and solid surface are intersected. During movement of the triple line on the solid surface, triple line has the chance to contacts with some spots with higher surface energy and sticks to them. This stoppage of the triple line is called pinning effect which affects the interface shape [20] Faster movement of triple lines observed during the drainage process decreases the chance of pinned triple line compared with slower movement of triple line observed during imbibition, causing similar receding contact angles during repeated tests. However, slower movement of triple line observed during the imbibition process causes stick-slip behavior of the interface and wider range of the contact angle. Khishvand et al. [30] have also reported a wide range of contact angles during the imbibition process using micro-CT tomography and indicated that roughness and different minerals on the surface are the main reasons for such wide variations in contact angles.

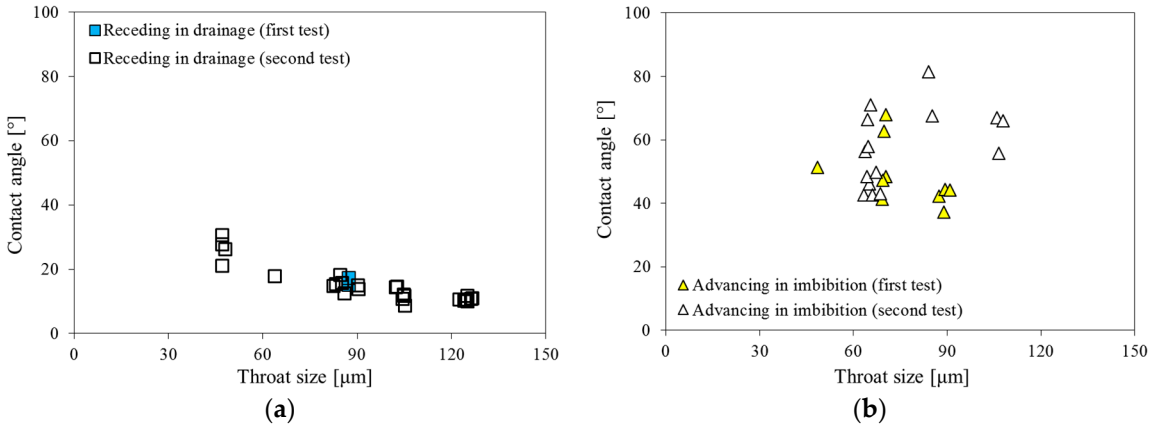

Figure 3. Dynamic contact angles during drainage and imbibition processes. (**a**) Receding contact angle, (**b**) Advancing contact angle.

Pore throat size. Receding contact angles increase with decreasing pore throat size (Figure 3a), in agreement with previous studies [32,47]. Li et al. [32] have reported that the contact angle increases when smaller capillary tubes are used. Using X-ray CT images, Tudek et al. [47] have observed that CO_2 bubbles trapped in smaller pores of a sandstone have higher contact angles due to local higher pressure of CO_2 in small pores. Results of pore-network numerical models have also shown higher advancing contact angle with smaller pore size for a flooded carbonated rock sample [48].

Receding contact angle (RCA) and advancing contact angle (ACA). Figure 4 shows the average and standard deviation of RCA and ACA varying with throat size. In this work, both dynamic contact angles are observed during both drainage and imbibition processes based on the interface direction. For example, when a trapped CO_2 bubble moves from the right side to the left side in the pore throat, right and left sides of CO_2 bubbles could be at advancing and receding contact angle, respectively (Figure 2). Our results show that RCA is highly reproducible regardless of pore throat size (Figure 4a). However, ACA shows high discrepancies (Figure 4b). This could be explained by the pinning effect of a triple line [20]. These results imply that the status of interface direction is more critical for defining

RCA and ACA and it is not true that every contact angle in drainage and imbibition phase are RCA and ACA, respectively.

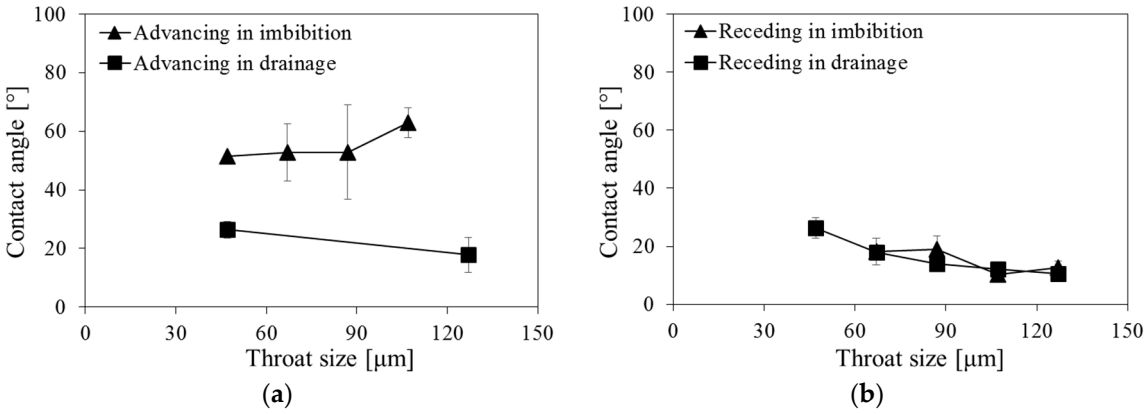

Figure 4. Dynamic contact angles during drainage and imbibition processes. (**a**) Receding contact angle, (**b**) Advancing contact angle.

Moreover, while RCA is almost independent of injection pattern (Figure 4a), ACA shows higher values during the imbibition process than that those measured during the drainage process (Figure 4b). As mentioned earlier, the observed slow movement of triple line during the imbibition process results in the pining effect which causes the increase in advancing contact angle.

3.2. Static Contact Angle

Static and equilibrium contact angles. Thermodynamically, the equilibrium contact angle (ECA) can only be measured at a global minimum free energy configuration, while the static contact angle (SCA) can be measured at any kinetically stable condition between advancing and receding configuration, which can be considered as a meta-stable equilibrium configuration [49]. In our micromodel, interface movement is stopped in two situations. First, before percolation of the fluids (CO_2 or water) into the micromodel (percolation occurs when the front of injected fluids reaches to the other side of the micromodel), some interfaces stop at smaller pore throats due to higher capillary pressure. Second, after percolation, because almost all the injected fluid passes through the percolation path, other interfaces remain motionless. In any of these situations, static contact angles (SCA) could be measured with the motionless interfaces. However, the system of the micromodel is under fluid (water or CO_2) injection continuously. Thus, the motionless interfaces are not allowed to rest and completely approach ECA. This is the reason for low reproducibility of SCA presented in Figure 5. Because of different level of relaxation of the interfaces, various mode of interfaces before stoppage (i.e., receding or advancing), and pinning effect originated from solid surface imperfection, SCA shows wide range of values for the two different tests and also for each test in any throat sizes. The range of SCA at each pore throat size is higher than that of equilibrium contact angle (ECA) measured with CO_2 or water droplet on flat surface (i.e., 8° to 45° on silica or glass surface) [18,22,43,50–52].

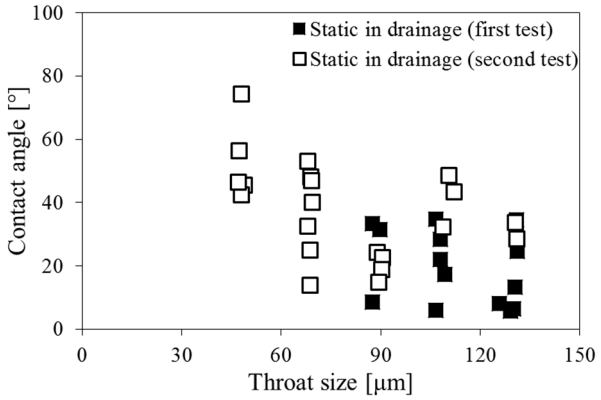

Figure 5. Static contact angle for two repeated tests at pressure of eight megapascals.

Static contact angle during drainage and imbibition processes. Figure 6 shows the effect of injection condition (i.e., drainage and imbibition) on average and standard deviation of static contact angle (SCA) measured at pressure of one or eight megapascals. The motionless interfaces before stoppage can be in any dynamic mode of advancing or receding. After stoppage, the shape of motionless interface is close to its dynamic mode before stoppage. Since the majority of interfaces are in receding mode during drainage, most of SCA measured in drainage behave similar to RCA. The results show SCA measured during drainage is increased with reducing pore throat size, similar to the trend observed for RCA. However, because a minority of the interfaces are in advancing mode before stoppage, the trend is not as clear as the RCA trend and reproducibility is lower.

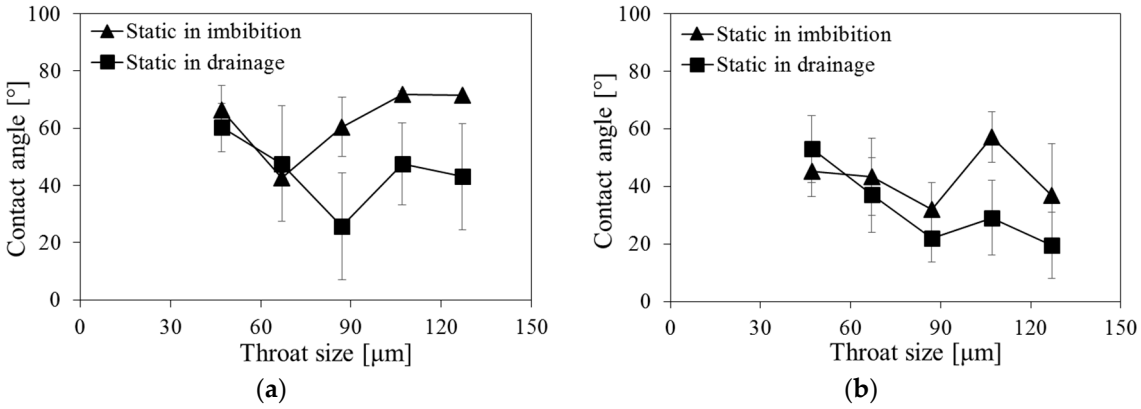

Figure 6. Average and standard deviation of static contact angle during drainage & imbibition processes. (**a**) At pressure of one megapascal; (**b**) At pressure of eight megapascals.

In the same way, because majority of interfaces are in advancing mode during imbibition, the value of SCA measured during imbibition is close to ACA. As shown in Figure 6, there are no distinguishable relations between SCA measured during imbibition process and pore throat size, consistent with ACA results of the present study. Moreover, SCA measured during imbibition are higher than those measured during drainage process at pressure of one or eight megapascals. Khishvand et al. [30] have also observed that contact angle is increased when injection phase is switched from drainage to imbibition.

According to Figure 6, when pore throat size is small (i.e., less than 90 µm), the values of SCA during drainage and those measured during imbibition become close to each other. When CO_2 injection stops, water tends to move back into smaller pore throats due to wetting characteristic [6], causing smaller pore throats to mostly become under the advancing condition. Therefore, SCAs

measured during both imbibition and drainage processes are similar to each other when pore throat sizes are small.

4. Analysis

4.1. Comparing Different Types of Contact Angle

Figure 7 shows the average and standard deviation of all contact angles (RCA, ACA, and SCA) measured in this study. These results show that SCA, RCA, and ACA have high discrepancies at each pore throat size, consistent with previous studies [38,40,47]. Contact angles measured using micro-CT with rock cores and beads packs also have a wide range of values due to hysteresis of contact angle, exposure time, complex geometry, and physical and chemical heterogeneity of the surface [38,40,47].

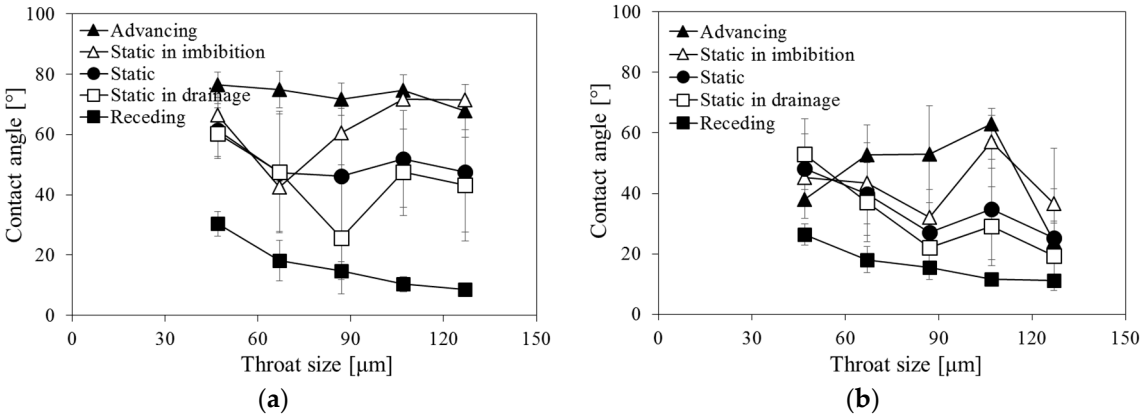

Figure 7. Average and standard deviation of advancing contact angles (ACA), receding contact angles (RCA), and static contact angles (SCA) during drainage and imbibition processes. (**a**) At pressure of one megapascal; (**b**) At pressure of eight megapascals.

It is important to choose a proper value among various types of contact angles in order to estimate the wettability behavior of rock formation and sealing caprock. RCA is the lower boundary of contact angle. It can be used to determine injectability and capillary pressure for CO_2 injection into CO_2 storage. RCA should also be considered to determine CO_2 resistivity of the caprock (or capillary breakthrough pressure at the caprock) using Young–Laplace equation (Equations (3) or (4)).

Limitations in measuring dynamic contact angle, especially in situ measurement at pore-scale, have forced researchers to focus on SCA. However, static contact angle is of minor importance in comparison with dynamic contact angle for geological sequestration. SCA is suitable for stable conditions when there is no motion in the interface of fluids. The danger of leakage increases when CO_2 starts to move. Moreover, flow regime and sweep efficiency, which determine the capacity of storage, depend on dynamic parameters, including capillary number and viscosity (or mobility) ratio [53]. Dynamic contact angle has an important role in capillary number value.

4.2. Pressure Effect on Contact Angle

Jung and Wan [51] have reported that equilibrium contact angle increases with the depth of storage. This could result in possible CO_2 leakage. However, RCA is more critical for evaluation of CO_2 resistivity of the caprock as mentioned in Section 4.1. Figure 8 shows that RCA at one megapascal is similar to that at eight megapascals where CO_2 exists as gas or liquid. This implies that the effect of wettability with increased depth of CO_2 storage on the risk of CO_2 leakage can be disregarded. However, pore sizes reduce with the increase of depth and effective stress resulting in rise of the breakthrough capillary pressure based on Young–Laplace's equation (Equation (3) or Equation (4)).

It is noteworthy that the effect of temperature is not considered here. For a comprehensive study, temperature effect and changing the CO_2 state into supercritical condition should be taken into account.

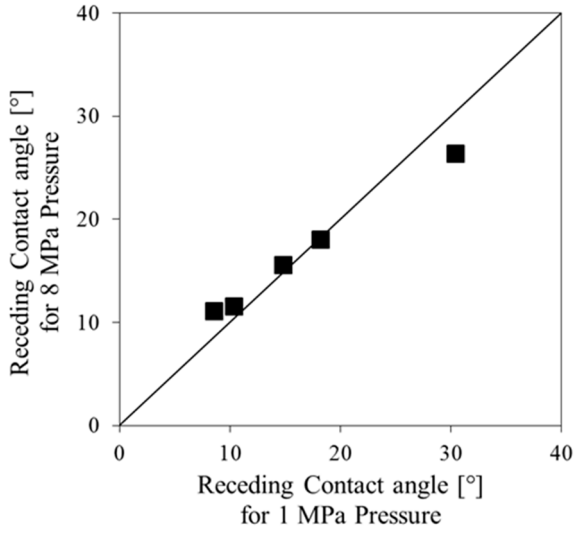

Figure 8. Receding contact angle at pressure of eight megapascals vs. that at pressure of one megapascal.

4.3. Contact Angle Hysteresis

Potential mobility of CO_2 bubble. Figure 9 shows a disconnected bubble of CO_2 trapped by water inside a pore throat. When the pressure at the right side (P_{water1}) increases gradually and becomes higher than a threshold value, the CO_2 starts to move toward the left side. At this point, both ACA and RAC could be measured on right and left sides of a CO_2 bubble.

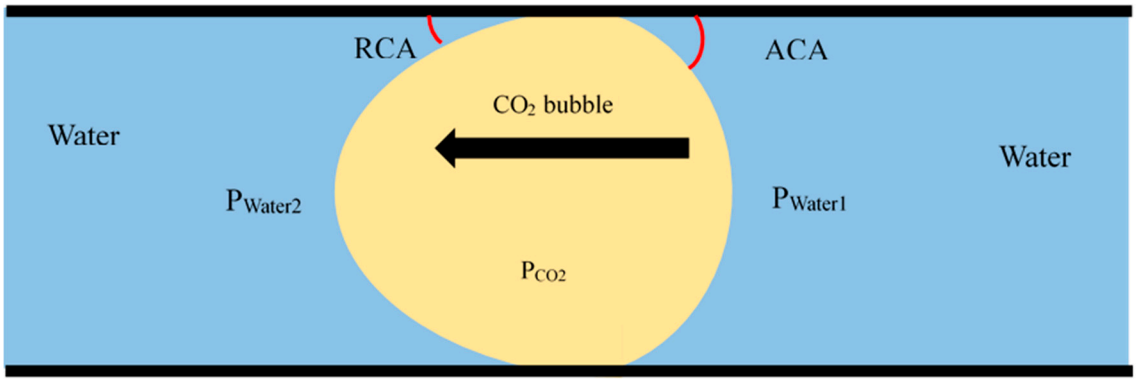

Figure 9. A disconnected bubble of CO_2 trapped by brine capillary or residual trapping.

The capillary pressure in the right and left interface can be defined as below (Equations (1) and (2), respectively).

$$P_{capillary\ 1} = P_{CO_2} - P_{water\ 1} \quad (1)$$

$$P_{capillary\ 2} = P_{CO_2} - P_{water\ 2} \quad (2)$$

where $P_{capillary1}$ is the capillary pressure in the right water–CO_2 interface, $P_{capillary2}$ is the capillary pressure in the left water–CO_2 interface, P_{CO_2} is the pressure inside the CO_2 bubble, P_{water1} is the water pressure in the right side (where water advances), and P_{water2} is the pressure in the left inside (where water recedes).

By subtracting Equation (2) from Equation (1), Equation (3) is resulted.

$$P_{water\ 1} - P_{water\ 2} = P_{capillary\ 2} - P_{capillary\ 1} \quad (3)$$

From Young–Laplace's equation:

$$P_{capillary\ 1} = \frac{2\gamma \cos(ACA)}{r} \quad (4)$$

$$P_{capillary\ 2} = \frac{2\gamma \cos(RCA)}{r} \quad (5)$$

By subtracting Equations (4) and (5) from Equation (3):

$$P_{water1} - P_{water2} = \frac{2\gamma}{r} [\cos(RCA) - \cos(ACA)] \quad (6)$$

According to Equation (6), by an increase of the dynamic contact angle hysteresis (defined as the difference between RCA and ACA), higher water pressure difference is required before CO_2 migration. In other words, mobility of the CO_2 decreases as the hysteresis increases.

Figure 10 presents contact angle hysteresis for dynamic and static contact angles. The hysteresis of the contact angle generally increases with increasing pore throat size. The hysteresis of a dynamic contact angle at eight megapascals is lower than that at one megapascal. This implies that the mobility potential of a CO_2 bubble increases with increasing CO_2 storage depth when the pore throat size is constant. However, as the depth of CO_2 storage increases, pores throat size decreases due to higher effective stress [50]. According to Equation (6), when deeper aquifer site is selected for CO_2 storage, higher capillary pressure is expected due to smaller pore throat size. However, the negative effect of lower hysteresis on the contact angle should be considered for the mobility of trapped CO_2 bubble.

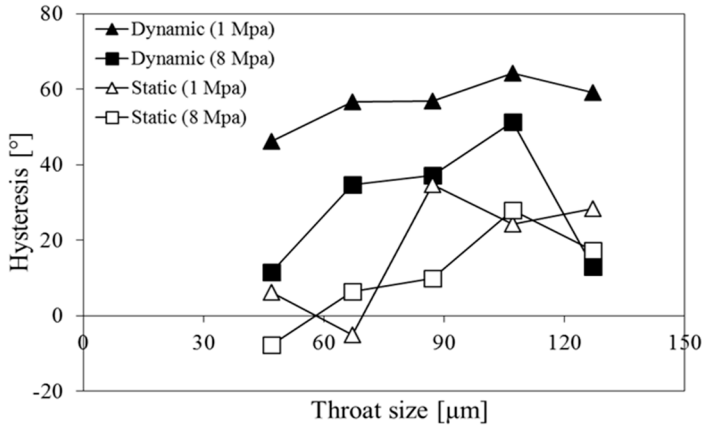

Figure 10. Contact angle hysteresis (dynamic contact angle hysteresis = ACA − RCA, static contact angle hysteresis = SCA in imbibition − SCA in drainage).

Relative permeability. Relative permeability is defined as a dimensionless measurement of effective permeability of a phase in a multi-phase flow system. Thus, hysteresis of relative permeability can be observed during the injection of alternate fluids (water and CO_2) into porous media [54]. The relative permeability of non-wetting phase (CO_2) during imbibition is known to be lower than that during drainage [55]. This is due to the following two facts: (1) contact angle hysteresis (the difference between ACA and RCA) influences the relative permeability, implying that factors affecting contact angle hysteresis such as pressure, and pore throat size should be considered to select the relative permeability in numerical simulation; and (2) the presence of trapped non-wetting phase (CO_2) influences the flow path of wetting fluid (water). When trapped non-wetting phase (CO_2) occupies

larger pores, it causes the injected wetting fluid (water) to change its flow paths, resulting in decreased relative permeability [56]. Spiteri et al. [57] have performed numerical modelling of a Water Alternating Gas (WAG) system for CO_2 sequestration and shown favorable results for residual trapping due to relative permeability hysteresis by decreasing leakage risk through lowering the accumulation of CO_2 plum under caprock.

4.4. Comparing Contact Angle of Bubbles on Flat Surface with Contact Angle of the Interfaces Covering Pore Throat Inside Pores

In the literature, mostly contact angles have been measured with a CO_2 (or water) droplet on a flat surface. In the same way and with the similar fluid system configuration, static contact angle on a flat surface inside the micromodel can be measured (Figure 11).

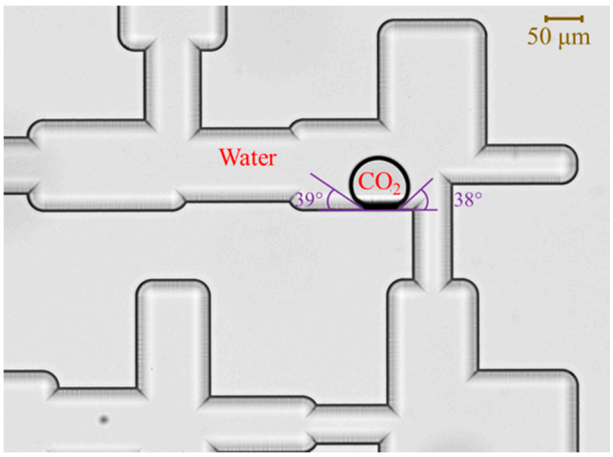

Figure 11. Contact angle measurement inside the micromodel on a flat surface of a channel (one megapascal pressure).

Contact angle of bubbles on the flat surface inside micromodel. Figure 12 shows all type of contact angles measured in this study with the interface covering throat as well as contact angle of small bubbles on the flat surface inside micromodels. Our results reveal that a contact angle on the flat surface is not directly affected by pore throat size. However, in the Figure 12, the contact angles of the bubbles are shown with red dots (this is shown against throat size only to show the location of measurement).

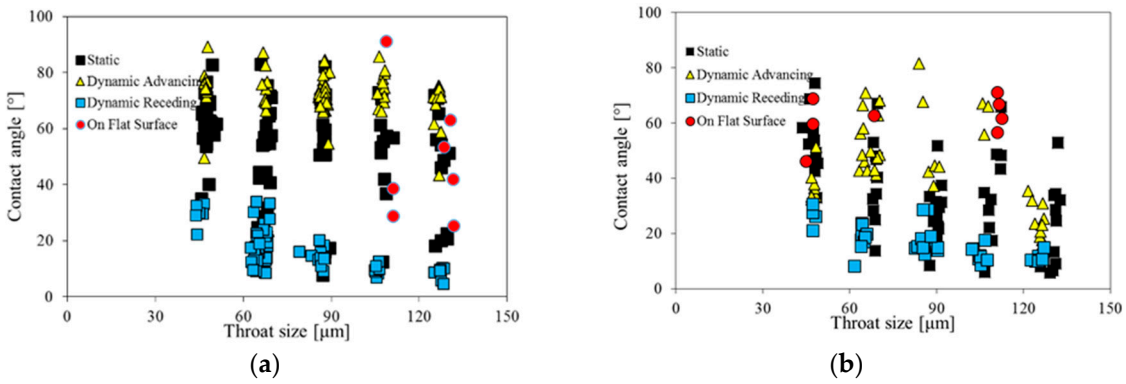

Figure 12. Range of contact angle values according to various pore throat sizes. (**a**) At pressure of one megapascal; (**b**) At pressure of eight megapascals.

Average contact angles on flat surface inside micromodel at pressure of one and eight megapascals are 62° ± 7° and 49° ± 21°, respectively, in agreement with Kim et al. [58] observations showing a wide range of contact angles from 40° to 80° inside a uniform micromodel. Contact angles on a flat surface in this study are higher than those shown in previous sessile drop or captive bubble tests with large droplet of water or bubble of CO_2 (i.e., 8° to 45° on silica or glass surface) [18,22,43,50–52]. This could be due to the micro-scaled CO_2 bubble size on a flat surface inside the micromodel of the present study in comparison with the other studies with larger dimension of bubble ranging from a few to tens of millimeter. Shojai Kaveh et al. [59] have reported that smaller bubbles have higher contact angles in comparison with larger ones as a result of buoyancy force. Previous studies have also shown that contact angles on a flat surface of rocks are smaller than those measured inside rock pores using X-ray tomography method due to gravity and buoyancy [40,47]. These results indicate the important conclusion that glass (or rock) in pore-scale are as water-wet as already recognized by conventional macro-scale measurement.

Capillary or residual trapping. In capillary or residual trapping, CO_2 bubbles are entrapped inside rock pores by three mechanisms: (1) snap-off, (2) dead-end, and (3) by-passing. In snap-off, when water is invaded into a water-wet media, the water in the corner of a throat will swell gradually until it disconnects the non-wetting phase in the throat and forcibly pushes non-wetting into pore bodies [60,61]. The snap-off trapping mechanism is dominant for water-wet rocks with a high aspect ratio of pore-body diameter to pore-throat diameter [62]. The snap-off mechanism starts when the non-wetting phase (CO_2) fills the pore throat first. The water layer in the corner then swells by water injection until it completely separates the non-wetting phase (CO_2) from the rock surface, similar to a bubble resting on a flat surface inside the micromodel as shown in Figure 11. In the dead-end, the non-wetting phase (CO_2) is trapped in dead-end pores that it carries no flow. By-passing can be defined by a pore-doublet model. When two tubes with different sizes are branched and rejoined, non-wetting fluid is trapped in the larger tube. Thus, wetting phase by-passes the larger tube and passes through the smaller tube. For both dead-end and by-passing trapping mechanisms, the water-CO_2 interface covers whole the pore throat. Thus, contact angles measured inside the micromodel can give more realistic values for numerical simulations compared with a contact angle of a bubble/droplet measured on a flat surface.

5. Conclusions

Capacity and safety prediction of geological CO_2 sequestration require a realistic wettability behavior to model multiphase immiscible fluid flow. In this paper, a new method of pore-scale contact angle measurement was presented. A series of dynamic and static contact angles were determined inside a high-pressure glass micromodel with randomly patterned channels. In addition, contact angles of CO_2 bubbles on flat surfaces of micromodel channel were measured for comparison. Results observed in this study are summarized below:

(1) Although contact angles are measured inside a highly smooth and chemically homogenous glass micromodel, a wide range of pore-scale contact angles are observed in our results, implying the complexity of the pore-scale contact angle. Thus, higher discrepancy in the contact angle is plausibly expected in real rocks containing various minerals with high roughness, irregular shape pores, and various pore throat sizes.

(2) Receding contact angle (RCA) shows more reproducibility than advancing contact angle (ACA) or static contact angle (SCA). This higher reproducibility is observed for each throat size and in repeated tests. The lower reproducibility for ACA and SCA could be due to the pinning effect of the triple line.

(3) Both RCA and ACA can occur during both drainage and imbibition processes. RCA shows more reproducibility even during different patterns of injections (i.e., drainage and imbibition).

(4) By decreasing pore size from 127 μm to 47 μm, RCA increases from 11° to 26° at pressure of eight megapascals and from 9° to 30° at pressure of one megapascal. Local constrictions increase the pressure inside CO_2 bubbles in the small pores resulting in an increase of the interfaces curvature.

(5) Generally, SCA during imbibition is higher than SCA during drainage. SCA is close to the dynamic contact angle (receding or advancing) before interface stops.

(6) Although SCA is not as reproducible as RCA, it shows an increasing trend with decreasing pore throat sizes from 25° to 48° at pressure of eight megapascals and from 52° to 62° at pressure of one megapascal pressure during drainage.

(7) RCA and ACA are lower boundaries of contact angles while SCA rests between them. The upper boundary is not as distinct as the lower one due to the pinning effect.

(8) Hysteresis of dynamic contact angle (ACA—RCA) is higher at pressure of one megapascal than that at pressure of eight megapascals. A CO_2 bubble has higher mobility in larger depths due to lower hysteresis which is unfavorable. However, higher density of CO_2 requires its injection in deep depths (800~2000 m).

(9) Contact angle of CO_2 bubbles resting on the flat surface of the micromodel channel show a wide range from 40° to 80°. Its average values at pressure of one and eight megapascals are 62° and 49°, respectively. These contact angles are much higher than those observed with sessile drop or captive bubble test on a flat plate of glass in the literature. Our results are not affected by gravity or buoyancy due to the micro-scale dimensions of the CO_2 bubble.

Our measurement method can also be applied in pore-scale models for a wide range of problems involving multiphase fluid flow in porous media, such as enhanced oil/gas recovery and methane extraction from methane-hydrate-bearing sediments.

Acknowledgments: This research was supported by Basic Science Research Program through the National Research Foundation of Korea (NRF) funded by the Ministry of Education (2017R1D1A3B03031369).

Author Contributions: Mohammad Jafari and Jongwon Jung conceived, designed, and performed the experiments. Mohammad Jafari and Jongwon Jung analyzed the data and wrote the paper. All authors read and approved the final manuscript.

Conflicts of Interest: The authors declare no conflict of interest.

References

1. Jafari, M.; Cao, S.C.; Jung, J. Geological CO_2 sequestration in saline aquifers: Implication on potential solutions of China's power sector. *Resour. Conserv. Recycl.* **2016**, *121*, 137–155. [CrossRef]
2. Bachu, S. Sequestration of CO_2 in geological media: criteria and approach for site selection in response to climate change. *Energy Convers. Manag.* **2000**, *41*, 953–970. [CrossRef]
3. Wildenschild, D.; Armstrong, R.T.; Herring, A.L.; Young, I.M.; Carey, J.W. Exploring capillary trapping efficiency as a function of interfacial tension, viscosity, and flow rate. *Energy Procedia* **2011**, *4*, 4945–4952. [CrossRef]
4. Benson, S.M.; Cole, D.R. CO_2 sequestration in deep sedimentary formations. *Elements* **2008**, *4*, 325–331. [CrossRef]
5. Benson, S.; Cook, P.; Anderson, J.; Bachu, S.; Nimir, H.B.; Basu, B.; Bradshaw, J.; Deguchi, G. Underground geological storage. *Ipcc* **2005**, 195–276.
6. Krevor, S.; Blunt, M.J.; Benson, S.M.; Pentland, C.H.; Reynolds, C.; Al-Menhali, A.; Niu, B. Capillary trapping for geologic carbon dioxide storage–From pore scale physics to field scale implications. *Int. J. Greenh. Gas Control* **2015**, *40*, 221–237. [CrossRef]
7. Kimbrel, E.H.; Herring, A.L.; Armstrong, R.T.; Lunati, I.; Bay, B.K.; Wildenschild, D. Experimental characterization of nonwetting phase trapping and implications for geologic CO_2 sequestration. *Int. J. Greenh. Gas Control* **2015**, *42*, 1–15. [CrossRef]
8. Intergovernmental Panel on Climate Change. *Special Report on Carbon Dioxide Capture and Storage: Prepared by Working Group III of the Intergovernmental Panel on Climate Change*; Intergovernmental Panel on Climate Change: Geneva, Switzerland, 2005.

9. Scanziani, A.; Singh, K.; Blunt, M.J.; Guadagnini, A. Automatic method for estimation of in situ effective contact angle from X-ray micro tomography images of two-phase flow in porous media. *J. Colloid Interface Sci.* **2017**, *496*, 51–59. [CrossRef] [PubMed]
10. Alghunaim, A.; Newby, B.M.Z. Influence of tube wettability on water contact angle of powders determined by capillary rise. *Colloids Surfaces A Physicochem. Eng. Asp.* **2016**, *492*, 79–87. [CrossRef]
11. Alghunaim, A.; Kirdponpattara, S.; Newby, B.M.Z. Techniques for determining contact angle and wettability of powders. *Powder Technol.* **2016**, *287*, 201–215. [CrossRef]
12. Liu, Z.; Yu, X.; Wan, L. Capillary rise method for the measurement of the contact angle of soils. *Acta Geotech.* **2016**, *11*, 21–35. [CrossRef]
13. Labajos-Broncano, L.; González-Martín, M.L.; Bruque, J.M.; González-García, C.M. Comparison of the Use of Washburn's Equation in the Distance–Time and Weight–Time Imbibition Techniques. *J. Colloid Interface Sci.* **2001**, *233*, 356–360. [CrossRef] [PubMed]
14. Kwok, D.Y.; Budziak, C.J.; Neumann, A.W. Measurements of Static and Low Rate Dynamic Contact Angles by Means of an Automated Capillary Rise Technique. *J. Colloid Interface Sci.* **1995**, *173*, 143–150. [CrossRef]
15. Herring, A.L.; Sheppard, A.; Andersson, L.; Wildenschild, D. Impact of wettability alteration on 3D nonwetting phase trapping and transport. *Int. J. Greenh. Gas Control* **2016**, *46*, 175–186. [CrossRef]
16. Amott, E. Observations Relating to the Wettability of Porous Rock. *Pet. Trans. AIME* **1958**, *216*, 156–162.
17. Donaldson, E.C.; Thomas, R.D.; Lorenz, P.B. Wettability Determination and Its Effect on Recovery Efficiency. *SPE J.* **1969**, 13–20. [CrossRef]
18. Broseta, D.; Tonnet, N.; Shah, V. Are rocks still water-wet in the presence of dense CO_2 or H_2S? *Geofluids* **2012**, *12*, 280–294. [CrossRef]
19. Wan, J.; Kim, Y.; Tokunaga, T.K. Contact angle measurement ambiguity in supercritical CO_2-water-mineral systems: Mica as an example. *Int. J. Greenh. Gas Control* **2014**, *31*, 128–137. [CrossRef]
20. Jafari, M.; Jung, J. The change in contact angle at unsaturated CO_2-water conditions: Implication on geological carbon dioxide sequestration. *Geochem. Geophys. Geosyst.* **2016**, *17*, 3969–3982. [CrossRef]
21. Jung, J.; Hu, J.W. Impact of Pressure and Brine Salinity on Capillary Pressure-Water Saturation Relations in Geological CO_2 Sequestration. *Adv. Condens. Matter Phys.* **2016**, *2016*. [CrossRef]
22. Chiquet, P.; Broseta, D.; Thibeau, S. Wettability alteration of caprock minerals by carbon dioxide. *Geofluids* **2007**, *7*, 112–122. [CrossRef]
23. Chiquet, P.; Broseta, D.; Thibeau, S. Capillary Alteration of Shaly Caprocks by Carbon Dioxide. *SPE J.* **2005**, *94183*, 1–10. [CrossRef]
24. Kwok, D.Y.; Gietzelt, T.; Grundke, K.; Jacobasch, J.; Neumann, A.W. Contact angle measurement and contact angle interpretation. *Langmuir* **1997**, *13*, 2880–2894. [CrossRef]
25. Saghafi, A.; Javanmard, H.; Pinetown, K. Study of coal gas wettability for CO_2 storage and CH4 recovery. *Geofluids* **2014**, *14*, 310–325. [CrossRef]
26. Bikkina, P.K. Contact angle measurements of CO_2-water-quartz/calcite systems in the perspective of carbon sequestration. *Int. J. Greenh. Gas Control* **2011**, *5*, 1259–1271. [CrossRef]
27. Li, X.; Fan, X. International Journal of Greenhouse Gas Control Effect of CO_2 phase on contact angle in oil-wet and water-wet pores. *Int. J. Greenh. Gas Control* **2015**, *36*, 106–113.
28. Rao, D.N.; Girard, M.G. A new technique for reservoir wettability characterization. *J. Can. Pet. Technol.* **1996**, *35*, 31–39. [CrossRef]
29. Ramé, E. The Interpretation of Dynamic Contact Angles Measured by the Wilhelmy Plate Method. *J. Colloid Interface Sci.* **1997**, *185*, 245–251. [CrossRef]
30. Khishvand, M.; Alizadeh, A.H.; Piri, M. In-situ characterization of wettability and pore-scale displacements during two- and three-phase flow in natural porous media. *Adv. Water Resour.* **2016**, *97*, 279–298. [CrossRef]
31. Lin, T.S.; Zeng, Y.H.; Tsay, R.Y.; Lin, S.Y. Deflation rate dependence of receding contact angle on polymeric surfaces. *J. Taiwan Inst. Chem. Eng.* **2015**, *61*, 26–31. [CrossRef]
32. Li, X.; Fan, X.; Brandani, S. Difference in pore contact angle and the contact angle measured on a flat surface and in an open space. *Chem. Eng. Sci.* **2014**, *117*, 137–145. [CrossRef]
33. Lv, P.; Liu, Y.; Wang, Z.; Liu, S.; Jiang, L.; Chen, J.; Song, Y. In Situ Local Contact Angle Measurement in a CO_2-Brine-Sand System Using Microfocused X-ray CT. *Langmuir* **2017**, *33*, 3358–3366. [CrossRef] [PubMed]
34. Wildenschild, D.; Sheppard, A.P. X-ray imaging and analysis techniques for quantifying pore-scale structure and processes in subsurface porous medium systems. *Adv. Water Resour.* **2013**, *51*, 217–246. [CrossRef]

35. Andrew, M.; Bijeljic, B.; Blunt, M.J. Pore-scale imaging of trapped supercritical carbon dioxide in sandstones and carbonates. *Int. J. Greenh. Gas Control* **2014**, *22*, 1–14. [CrossRef]
36. Armstrong, R.T.; Georgiadis, A.; Ott, H.; Klemin, D.; Berg, S. Critical capillary number: Desaturation studied with fast X-ray computed microtomography. *Geophys. Res. Lett.* **2014**, *41*, 55–60. [CrossRef]
37. Andrew, M.; Bijeljic, B.; Blunt, M.J. Pore-by-pore capillary pressure measurements using X-ray microtomography at reservoir conditions: Curvature, snap-off, and remobilization of residual CO_2. *Water Resour. Res.* **2014**, *50*, 8760–8774. [CrossRef]
38. Andrew, M.; Bijeljic, B.; Blunt, M.J. Pore-scale contact angle measurements at reservoir conditions using X-ray microtomography. *Adv. Water Resour.* **2014**, *68*, 24–31. [CrossRef]
39. Lv, P.; Huang, Q.; Jiang, L.; Song, Y.; Liu, Y. Pore-scale contact angle measurements of CO_2-brine-glass beads system using micro-focused X-ray computed tomography. *Micro Nano Lett.* **2016**, *11*, 524–527. [CrossRef]
40. Klise, K.A.; Moriarty, D.; Yoon, H.; Karpyn, Z. Automated contact angle estimation for three-dimensional X-ray microtomography data. *Adv. Water Resour.* **2016**, *95*, 152–160. [CrossRef]
41. Williams, D.L.; Kuhn, A.T.; Amann, M.A.; Hausinger, M.B.; Konarik, M.M.; Nesselrode, E.I. Computerised measurement of contact angles. *Galvanotechnik* **2010**, *101*, 2502–2512.
42. Lamour, G.; Hamraoui, A.; Buvailo, A.; Xing, Y.; Keuleyan, S.; Prakash, V.; Eftekhari-Bafrooei, A.; Borguet, E. Contact angle measurements using a simplified experimental setup. *J. Chem. Educ.* **2010**, *87*, 1403–1407. [CrossRef]
43. Saraji, S.; Goual, L.; Piri, M.; Plancher, H. Wettability of supercritical carbon dioxide/water/quartz systems: Simultaneous measurement of contact angle and interfacial tension at reservoir conditions. *Langmuir* **2013**, *29*, 6856–6866. [CrossRef] [PubMed]
44. Arif, M.; Al-Yaseri, A.Z.; Barifcani, A.; Lebedev, M.; Iglauer, S. Impact of pressure and temperature on CO_2-brine-mica contact angles and CO_2-brine interfacial tension: Implications for carbon geo-sequestration. *J. Colloid Interface Sci.* **2016**, *462*, 208–215. [CrossRef] [PubMed]
45. Dettre, R.H.; Rulon, E.; Johnson, J. Contact Angle Hysteresis. IV. Contact Angle Measurements on Heterogeneous Surfaces. *J. Phys. Chem.* **1966**, *69*, 1507–1515. [CrossRef]
46. Tadmor, R. Line energy and the relation between advancing, receding, and Young contact angles. *Langmuir* **2004**, *20*, 7659–7664. [CrossRef] [PubMed]
47. Tudek, J.; Crandall, D.; Fuchs, S.; Werth, C.J.; Valocchi, A.J.; Chen, Y.; Goodman, A. In situ contact angle measurements of liquid CO_2, brine, and Mount Simon sandstone core using micro X-ray CT imaging, sessile drop, and Lattice Boltzmann modeling. *J. Pet. Sci. Eng.* **2017**, *155*, 3–10. [CrossRef]
48. Juri, J.E.; van Dijke, M.I.J.; Sorbie, K.S. Inversion of the lattice network wettability subjected to the capillary pressure of the entire flooding cycle: Hamiltonian Monte Carlo posterior sampling and prediction of the relative permeability. *J. Pet. Sci. Eng.* **2016**, *146*, 1037–1062. [CrossRef]
49. Ruiz-Cabello, F.J.M.; Rodríguez-Valverde, M.A.; Cabrerizo-Vílchez, M.A. Equilibrium contact angle or the most-stable contact angle? *Adv. Colloid Interface Sci.* **2014**, *206*, 320–327. [CrossRef] [PubMed]
50. Espinoza, D.N.; Santamarina, J.C. Water-CO_2-mineral systems: Interfacial tension, contact angle, and diffusionImplications to CO_2 geological storage. *Water Resour. Res.* **2010**, *46*, 1–10. [CrossRef]
51. Jung, J.; Wan, J. Supercritical CO_2 and Ionic Strength Effects on Wettability of Silica Surfaces: Equilibrium Contact Angle Measurements. *Energy & Fuels* **2012**, *26*, 6053–6059. [CrossRef]
52. Wang, S.; Edwards, I.M.; Clarens, A.F. Wettability phenomena at the CO_2-brine-mineral interface: Implications for geologic carbon sequestration. *Environ. Sci. Technol.* **2013**, *47*, 234–241. [CrossRef] [PubMed]
53. Lenormand, R.; Touboul, E.; Zarcone, C. Numerical models and experiments on immiscible displacements in porous media. *J. Fluid Mech.* **1988**, *189*, 165. [CrossRef]
54. Dernaika, M.R.; Kalam, M.Z.; Basioni, M.A.; Skjæveland, S.M. Hysteresis of Capillary Pressure, Resistivity Index and Relative Permeability in Different Carbonate Rock Types 1. 2012. Available online: http://jgmaas.com/SCA/2011/SCA2011-14.pdf (accessed on 7 December 2017).
55. Cao, S.C.; Dai, S.; Jung, J. Supercritical CO_2 and brine displacement in geological carbon sequestration: Micromodel and pore network simulation studies. *Int. J. Greenh. Gas Control* **2016**, *44*, 104–114. [CrossRef]
56. Juanes, R.; Spiteri, E.J.; Orr, F.M.; Blunt, M.J. Impact of relative permeability hysteresis on geological CO_2 storage. *Water Resour. Res.* **2006**, *42*, 1–13. [CrossRef]
57. Spiteri, E.J.; Juanes, R.; Blunt, M.J.; Orr, F.M. Relative-Permeability Hysteresis: Trapping Models and Application to Geological CO_2 Sequestration. *SPE Annu. Tech. Conf. Exhib.* **2005**. [CrossRef]

58. Kim, Y.; Wan, J.; Kneafsey, T.J.; Tokunaga, T.K. Dewetting of silica surfaces upon reactions with supercritical CO_2 and brine: Pore-scale studies in micromodels. *Environ. Sci. Technol.* **2012**, *46*, 4228–4235. [CrossRef] [PubMed]
59. Kaveh, N.S.; Rudolph, E.S.J.; van Hemert, P.; Rossen, W.R.; Wolf, K.-H. Wettability Evaluation of a CO_2 /Water/Bentheimer Sandstone System: Contact Angle, Dissolution, and Bubble Size. *Energy & Fuels* **2014**, *28*, 4002–4020. [CrossRef]
60. Saeedi, A.; Rezaee, R.; Evans, B. Experimental study of the effect of variation in in-situ stress on capillary residual trapping during CO_2 geo-sequestration in sandstone reservoirs. *Geofluids* **2012**, *12*, 228–235. [CrossRef]
61. Singh, K.; Menke, H.; Andrew, M.; Lin, Q.; Rau, C.; Blunt, M.J.; Bijeljic, B. Dynamics of snap-off and pore-filling events during two-phase fluid flow in permeable media. *Sci. Rep.* **2017**, *7*, 5192. [CrossRef] [PubMed]
62. Mackiewicz, S.M. Transport and Fate of a Lnapl in Fractured Clayey Till. Ph.D. Thesis, Iowa State University, Ames, IA, USA, 1994.